# Subthreshold and reverse bias model of graphene/p-type silicon Schottky diodes

Beltrán, Katty; Paredes, Jhon; Torres, F. Javier; Sánchez, Alfredo; Zambrano, César; Casalino, Maurizio; Prócel, Paul; Isabella, Olindo; Prócel, Luis Miguel

**DOI**
10.1016/j.jsamd.2025.100925

**Publication date**
2025

**Document Version**
Final published version

**Published in**
Journal of Science: Advanced Materials and Devices

**Citation (APA)**
Beltrán, K., Paredes, J., Torres, F. J., Sánchez, A., Zambrano, C., Casalino, M., Prócel, P., Isabella, O., & Prócel, L. M. (2025). Subthreshold and reverse bias model of graphene/p-type silicon Schottky diodes. *Journal of Science: Advanced Materials and Devices*, *10*(3), Article 100925. https://doi.org/10.1016/j.jsamd.2025.100925

Journal of Science: Advanced Materials and Devices 10 (2025) 100925

Contents lists available at ScienceDirect

Journal of Science: Advanced Materials and Devices

journal homepage: www.elsevier.com/locate/jsamd

Research article

# Subthreshold and reverse bias model of graphene/p-type silicon Schottky diodes

Katty Beltrán [a,*], Jhon Paredes [a,b], F. Javier Torres [c], Alfredo Sánchez [d], César Zambrano [c], Maurizio Casalino [e], Paul Prócel [f], Olindo Isabella [f], Luis Miguel Prócel [a,*]

[a] Instituto de Micro y Nano Electrónica, Universidad San Francisco de Quito, Diego de Robles S/N, 170901 Quito, Ecuador
[b] Toulouse INP, 2 Rue Charles Camichel, 31000 Toulouse, France
[c] Grupo de Química Computacional y Teórica, Universidad San Francisco de Quito, Diego de Robles S/N, 170901 Quito, Ecuador
[d] University of Delaware, 210 S College Ave, 170901 Newark, DE, USA
[e] Institute of Applied Science and Intelligent Systems "Eduardo Caianiello" - Unit of Naples (ISASI-CNR), Via Campi Flegrei, 34, 80078 Pozzuoli, Naples, Italy
[f] Delft University of Technology, Mekelweg 5, 2628 Delft, The Netherlands

ARTICLE INFO

*Keywords:*
Graphene–silicon interface
Schottky diode
p-type doping
Thermionic emission
Diffusion
Image-force lowering
Quantum mechanical analysis
Finite-element simulation
Subthreshold swing
Effective mass
Work function
Recombination velocity

ABSTRACT

This work presents a novel approach to studying, simulating, and modeling the graphene–silicon interface in Schottky diodes by integrating quantum-mechanical and device-level analyses. Such devices hold great performance potential in photodetecting, energy-harvesting, and sensing applications. Quantum-mechanical calculations determine key structural and electronic properties, such as the work function and effective mass, which are critical for understanding the interface's behavior. These parameters are then incorporated into finite-element simulations, solving the Poisson and Continuity equations to develop a subthreshold and reverse bias model for the graphene/p-type silicon Schottky device. The model characterizes J–V curves, identifying dominant electron transport mechanisms like thermionic emission and diffusion at varying recombination velocities. It also sheds light on the image-force lowering effect, which significantly impacts current density, especially under reverse bias conditions, by modulating the Schottky barrier height.

The model is validated by comparing the model with experimental data from graphene–silicon photodetectors, demonstrating its accuracy in predicting device performance. This approach offers valuable insights into optimizing any kind of Schottky diodes. By effectively bridging quantum-mechanical theory with practical device performance, the model proves to be a powerful tool for designing advanced semiconductor devices with enhanced efficiency and functionality, ensuring consistency from the atomistic to the device level.

## 1. Introduction

Since 2004, when graphene was successfully exfoliated from graphite, extensive research has been conducted on its different forms, including single-layer, bilayer, and multilayer graphene. This interest stems from graphene's remarkable properties, such as its high electron mobility, high capacity for electrical current transport, and low resistance, making it a promising candidate for next-generation field-effect transistors (FETs) [1–7]. Graphene is a classical Dirac semimetal, with linear energy–momentum dispersion near the Dirac points at the Fermi level. These Dirac cones, protected by symmetry in the absence of spin–orbit coupling, give rise to a number of unique electronic properties [8]. Moreover, researchers have successfully created metal–semiconductor junctions using single-layer graphene (SLG). A notable example is the fabrication of graphene–Si Schottky diodes, achieved by depositing exfoliated graphene onto silicon substrates [1]. These devices are currently employed in a wide range of applications in fields such as energy harvesting, chemical sensing, and optoelectronics [9]. Graphene possesses distinctive attributes, such as high optical transparency and excellent surface conductivity [2,3,7,10,11]; these characteristics allow graphene-based Schottky diodes to be employed in solar cells based on graphene–Si junctions and are gaining recognition due to their low-cost and straightforward fabrication methods [2,11]. Additionally, these devices are considered environmentally friendly [3,

* Corresponding authors.
*E-mail addresses:* kbeltran@estud.usfq.edu.ec (K. Beltrán), jparedes@estud.usfq.edu.ec (J. Paredes), jtorres@usfq.edu.ec (F.J. Torres), axs@udel.edu (A. Sánchez), czambrano@usfq.edu.ec (C. Zambrano), maurizio.casalino@na.isasi.cnr.it (M. Casalino), p.a.procelmoya@tudelft.nl (P. Prócel), o.isabella@tudelft.nl (O. Isabella), lprocel@usfq.edu.ec (L.M. Prócel).
Peer review under responsibility of Vietnam National University, Hanoi.

https://doi.org/10.1016/j.jsamd.2025.100925
Received 3 March 2025; Received in revised form 2 June 2025; Accepted 7 June 2025
Available online 19 June 2025

12]. In [12], graphene–Si Schottky junctions were successfully utilized in the fabrication of Schottky barrier solar cells (SBSC).

Graphene–Si Schottky diodes are also commonly used for gas sensing. Graphene's large active surface area and sensitivity to chemical adsorbates make these devices highly effective for detecting gases like $NO_2$, $H_2$, and other pollutants [13]. Gas sensing is enabled by variations in the forward bias current–voltage characteristics of the diode, which change with different gas concentrations and temperatures [14]. In [13,14], graphene–Si Schottky-based gas sensors were proposed for detecting $H_2S$ and $NO_2$, respectively. Both sensors demonstrated excellent performance, including high selectivity, reproducibility, and fast response times, confirming the suitability of graphene–Si Schottky diodes for this application. Additionally, these diodes have shown promise for humidity detection; [15] report a highly sensitive, selective, and multimode humidity sensor array based on a graphene–Si heterojunction, further broadening the environmental sensing applications of graphene–Si Schottky devices.

Another key application of the graphene–Si interface is in photodetector devices, owing to graphene's unique physical properties, high mobility, flexibility, and chemical stability [4,16,17], making it ideal for ultrafast, broadband, and flexible optoelectronics [18,19]. Photodetectors based on graphene–Si junctions show enhanced photoresponsivity [17,20], as graphene replaces metal contacts in Schottky junctions to form shallow junctions with an improved photoresponse. Likewise, its semimetallic nature and tunable Fermi level enable functionalities like bias-controlled detection [21,22]. Despite these advantages, graphene's intrinsically low optical absorption limits device efficiency. To address this, hybrid structures have been developed that significantly enhance performance. For example, the Graphene Charge-Coupled Device (GCCD) uses pre-avalanche multiplication and charge storage [20], while the Graphene–Oxide–Semiconductor (GOS) device achieves avalanche amplification via field-effect coupling [23]. Additionally, graphene's strong UV absorption supports long hot-carrier lifetimes and internal quantum efficiencies above 100% in silicon detectors [24], and functionalized forms like fluorinated graphene enable broadband detection from UV to infrared [25,26].

The previous optoelectronics study conducted in [27] provides relevant groundwork and serves as a case study for our work. In it, Schottky photodetectors (PDs) that operate with vertical illumination and exhibit enhanced resonant cavity behavior were fabricated, achieving efficient near-infrared (NIR) photodetection at 1550 nm. These devices have applications in fields ranging from optical communications to remote sensing. The PDs were fabricated on a p-type silicon substrate with a thickness of 200 μm, doped with a low boron concentration ($N_A \sim 10^{15}$ cm$^{-3}$). The findings provide a clear understanding of the devices' functionality and demonstrate rectifying I–V behavior consistent with the Schottky diode equation. However, a comprehensive understanding of the physics involved at the graphene–Si Schottky barrier has yet to be achieved.

Relevant TCAD work on the graphene–Si interface has been developed in [28,29]. In [28], highly rectifying C/p-type Si junctions were characterized by constructing and optimizing 2D and 3D models based on the measured I–V characteristics. Similarly, in [29], the performance of graphene–Si Schottky-based solar cells was analyzed using I–V curves and internal quantum efficiency to understand the devices' behavior. Both studies provide valuable insights and detailed results, contributing to the understanding of the underlying physics of the graphene–Si interface. However, there remains a need for a more detailed description of the interface at the atomistic level, which could offer a deeper understanding of the phenomena involved. Furthermore, establishing a stronger correlation between theoretical models and experimental data would be beneficial for aligning simulation results with real-world device performance.

In this work, a novel approach is taken to rigorously study and model the graphene–Si interface. An initial quantum-mechanical analysis of the interface in a crystal supercell is conducted to obtain basic electronic properties, such as work function, effective mass, and band structures. These results are then used in a finite element simulation to derive a TCAD-based model for the graphene/p-Si junction. The simulation outputs are subsequently compared and fitted to the experimental data in [27]. The final subthreshold and reverse bias model developed for graphene/p-Si Schottky diodes is characterized by its atomistic properties which are then employed in simulation to obtain the current density–voltage (J–V) curve. This multi-scale approach, which links quantum-mechanical modeling, device-level simulation, and experimental validation, provides a comprehensive framework that, to our knowledge, has not been reported in this form for graphene–Si Schottky diodes. Additionally, it significantly enhances the understanding of the underlying physical phenomena and current transport mechanisms at the junction.

Remarkably, although the graphene-based junctions analyzed in this work involve only p-type silicon, the study should be regarded as a versatile tool for investigating this class of junctions, regardless of the semiconductor type, specific experimental conditions, or fabrication process.

The remainder of this document is organized as follows: Section 2 presents the methodology employed, Section 3 exhibits the results of the quantum-mechanical analysis and the TCAD simulation along with the subthreshold and reverse bias model, and Section 4 compiles the primary observations and findings of this work, and also proposes potential subjects for future research.

## 2. Methodology

The methodology employed for the computational modeling, as illustrated in Fig. 1, is divided into two stages. In the first stage, a quantum-mechanical analysis of the interface is performed using the High-Performance Computing (HPC) server and Quantum-ATK software from Synopsys. The Density Functional Theory (DFT) is applied to approximate the solution to Schrödinger's equation and to obtain important physical parameters such as the work function, Fermi level, effective mass, and band structure.

The second stage involves the finite-element simulation of the interface. Here, the physical parameters obtained from the quantum-mechanical analysis, along with the device geometry, are used as input parameters in Synopsys Sentaurus software. At this stage, Poisson's equation, coupled with the drift–diffusion model and the continuity equation, is solved to obtain current density–voltage (J–V) curves and band diagrams characterizing the junction. The J–V curves are analyzed by exploring the mechanisms at the interface — thermionic emission, diffusion, and image-force lowering — while varying key parameters such as recombination velocity ($v_{rh}$) and interface resistance ($R$). Variations in $v_{rh}$ and $R$ result in significant changes to the J–V curve behavior, particularly in the subthreshold swing ($SS$) and current density magnitude ($J$). Additionally, band diagrams are studied to evaluate the effects of image-force lowering on Schottky barrier ($\Phi_B$) modulation. These analyses, which provide a detailed understanding of the parameter effects, are later employed to develop a comprehensive subthreshold and reverse bias model for the graphene/p-Si interface.

Finally, these results are fitted to the experimental data in [27] to further verify the validity and accuracy of the model.

### 2.1. Quantum mechanical calculations

The model for the quantum mechanical calculations was obtained by extending the unit cell of a [100] pure silicon surface (i.e., the most stable Si surface [30]) containing eight layers. The employed factors were 3 and 5 for the $a$ and $b$ directions, respectively. The latter resulted in a supercell model of 120 Si atoms, which was fully optimized (i.e., cell parameters and atomic positions) as a first step of the study. Subsequently, a monoatomic graphene sheet composed of 80 C atoms was placed onto the optimized silicon supercell to obtain

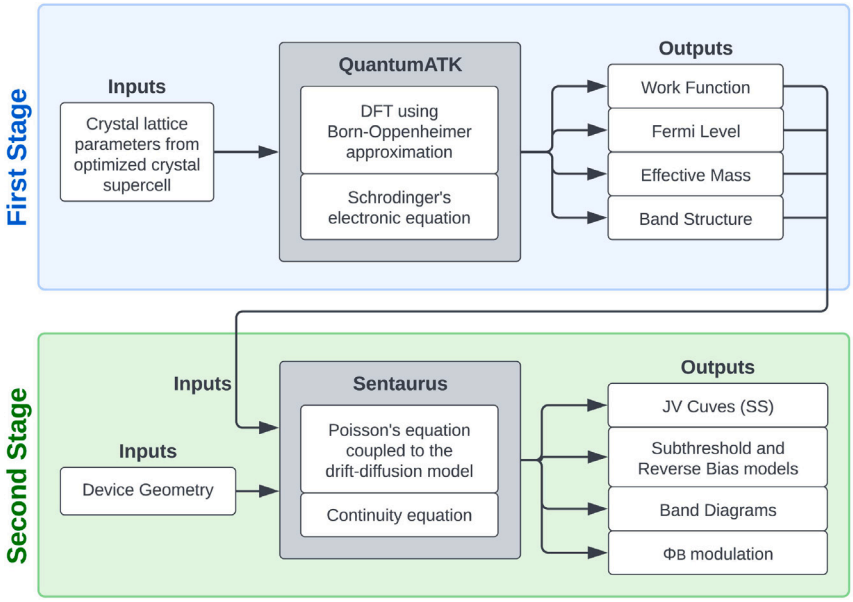


**Fig. 1.** Methodology Flow Diagram.

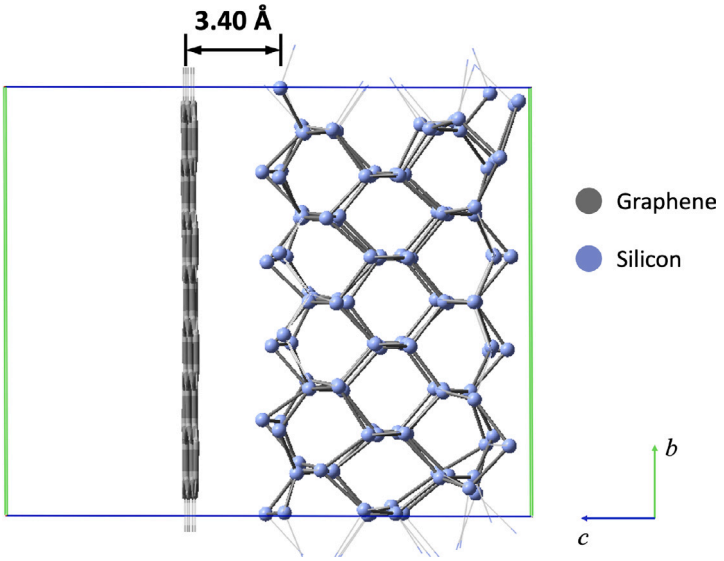


**Fig. 2.** Optimized crystal supercell.

the interface model. It must be noted that the procedure followed to construct the semiconductor–metal model for the quantum mechanical calculations resulted in a semi-ordered 2D–2D vertical van der Waals stacked silicon–graphene bilayer with a near-zero twist-angle [31] (see Fig. A.1(a) in Appendix A).

Upon the construction of the model, the strain forces resulting from the atomic interaction at the interface were minimized by means of a further optimization process where neither symmetry nor geometry constraints were imposed. As a result, the optimized structure is more accurately described as a turbostratic stacking system [32], where the carbon atoms maintain graphene's characteristic honeycomb arrangement while the silicon atoms adopt a less ordered distribution (see Fig. A.1(b) in Appendix A). The latter behavior can be attributed to the inherent mobility of the silicon [100] surface atoms located at the interface [30]. All the calculations at this stage of the study were conducted at the Perdew–Burke–Ernzerhof (PBE) [33,34] level as implemented in the VASP 5.4.4 software [35–38]. Moreover, the dispersive forces were copped by means of a Grimme-like pairwise potential [39]. The energy cutoff for the self-consistent field (SCF) calculations was set to 450 eV (as defined by an energy convergence test), and default values for geometry optimization and other control parameters were considered.

As exhibited in Fig. 2, the obtained model at equilibrium is an almost-rectangular cell with $a$ = 12.074945 Å, $b$ = 17.502307 Å, and $c$ = 21.364605 Å, with a vacuum of about 9 Å along the $c$ direction. Moreover, the distance between the Si surface and the graphene sheet is about 3.4 Å.

A crystallographic information file (CIF) containing the model can be found as supporting information. The latter was then exported to the QuantumATK software to compute the electronic properties that are required for the subsequent simulation at the device level, namely the work function, the electronic effective mass, the density of states, and the approximate bandgap. QuantumATK was used because it is tightly integrated with Sentaurus, the software used for the finite-elements model (see Section 2.2).

**Table 1**
Device measurements.

| Parameter | Value |
|---|---|
| Graphene thickness | 0.35 nm |
| Silicon thickness | 200 μm |
| Area | $\pi \times 10^4$ cm$^2$ |

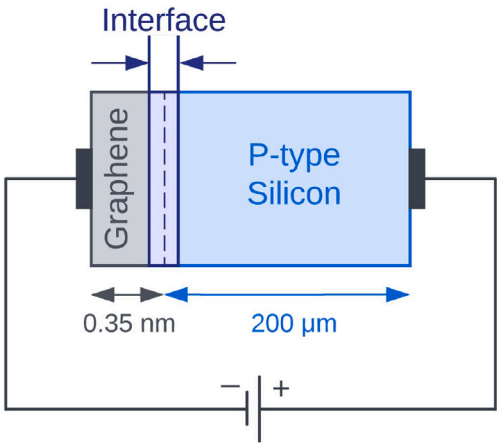


**Fig. 3.** Device schematic (not to scale) - Graphene/p-Si Schottky diode.

In a subsequent stage of the study, the model employed in QuantumATK was further modified to change the atomic distance at the interface, in order to assess the effect of changes in this distance on the electronic properties. Additionally, the band structure of the optimized graphene–Si configuration was compared to that of pristine graphene to highlight the impact of the interface interaction on the electronic properties.

### 2.2. Finite elements methods

A p-type Schottky device, doped with boron ($N_A \sim 10^{15}$ cm$^{-3}$), containing the graphene/p-Si interface was built in Sentaurus, following the measurements described in [27] (see Table 1). A schematic (not to scale) of the device is shown in Fig. 3. To accurately capture the physical behavior at the interface, a non-uniform meshing strategy was implemented. The mesh is highly refined in the vicinity of the interface, where key transport phenomena, such as thermionic emission–diffusion and the image-force-lowering effect, play a dominant role. A global refinement window was defined over the entire device area, enabling a gradual transition in mesh density. Within this window, a refinement function was applied that initiates with a fine mesh layer of 0.001 μm near the metal–silicon interface. The layer thickness then increases progressively by a factor of 1.1, up to a maximum of 0.25 μm laterally and 0.2 μm vertically toward the outer regions of the device. This graded mesh ensures fine resolution where it is most needed — near the interface — while maintaining computational efficiency in less critical areas.

The graphene material employed in the device was modeled using physical parameters — work function and effective mass — derived from quantum mechanical analysis. Additionally, resistivity and temperature-related parameters, including lattice thermal conductivity, lumped electron–hole–lattice heat capacity at 300 K, and the temperature coefficient, were obtained from [40–43].

The models employed for the aforementioned device in Sentaurus are described as follows.

Thermionic emission–diffusion theory was implemented in Sentaurus by activating the isothermal option. This model is described by (1) [44].

$$J_{TED} = \frac{qN_c v_{rh}}{1 + \frac{v_{rh}}{v_D}} e^{-\frac{q\phi_B}{kT}} \left( e^{\frac{qV}{kT}} - 1 \right) \tag{1}$$

where $J_{TED}$ is the thermionic emission–diffusion current density, $N_c$ is the effective density of states, $v_{rh}$ is the recombination velocity, $v_D$ is diffusion velocity, $\phi_B$ is the Schottky barrier height, $V$ is the applied voltage, $k$ is the Boltzmann constant, $T$ is the temperature, $q$ is the electron charge.

It must be noted that this model is limited under extreme temperature and high doping conditions. At low temperatures, thermionic emission is suppressed due to insufficient thermal energy, and tunneling (field emission, FE) or thermionic-field emission (TFE) becomes significant [44]. At high temperatures, the recombination velocity $v_{rh}$ becomes limited and eventually saturates due to the physical limit set by the thermal velocity ($\sim 10^7$ cm/s for Silicon) [44,45]. Besides this, for heavily doped semiconductors ($> 10^{18}$ cm$^{-3}$), the depletion width becomes very narrow, enhancing tunneling effects. In such cases, the semiconductor becomes degenerated, and the use of Fermi–Dirac statistics becomes necessary; this invalidates the model since it relies on the Maxwell–Boltzmann approximation.

Additionally, a sweep of $v_{rh}$ was performed to assess its contribution to the dominant current transport mechanism in the diode: thermionic emission versus diffusion. Eq. (1) establishes that when $v_{rh} \gg v_D$, the diffusion process becomes the limiting factor, and the saturation current density is given by $J_{TED} = J_D$ (diffusion current density). Contrary to this, when $v_D \gg v_{rh}$, thermionic emission dominates the transport mechanism and $J_{TED} = J_{TE}$ (thermionic emission current density) [44].

Moreover, depending on the dominant current transport mechanism, the subthreshold swing $SS$ may deviate from the standard value of 60 mV/dec. According to [44], when the dominant mechanism is not purely thermionic emission, ideality factor $\eta$ assumes a value greater than one to account for this effect. $\eta$ is introduced into the diode in (2).

$$J = J_0 \left[ e^{\frac{qV}{\eta kT}} - 1 \right] \tag{2}$$

where $J$ is the diode current density and $J_0$ is the saturation current density.

Eqs. (1) and (2) are relevant for Section 3.2 to analyze the results, providing insights into the behavior of the J–V curves, the underlying transport mechanisms, and the influence of the recombination velocity parameter ($v_{rh}$).

Next, the image-force lowering model in Sentaurus was applied to the device to analyze the bias dependent Schottky barrier $\Phi_B$ at the graphene/p-Si interface [46]. A Schottky barrier model is utilized for the metal–semiconductor junction, incorporating the reduction of the potential energy barrier due to the image force. The impact of the image-force lowering effect is examined through a parametric sweep of interface resistance $R$. The magnitude of the bias-dependent image-force lowering is defined in Sentaurus manual (refer to [47]).

In addition, due to the presence of series resistance in the TCAD simulations, an external 'compact model' was necessary to mitigate this effect and accurately graph and calculate subthreshold swings. This model was developed in MATLAB® and serves as an extrapolation of the data in subthreshold bias, which is described by the diode equation in (2). The compact model is used to preserve the subthreshold swing behavior typical of subthreshold bias in the forward bias regime, compensating for the series resistance and ensuring an accurate representation of the device's characteristics.

### 2.3. Experimental case study description

The fabrication process and geometry of the graphene–Si Schottky photodetector (PD) from [27], as displayed in Fig. 4, are described as follows:

First, a 100 nm $SiO_2$ layer is deposited onto a 200 μm-thick p-Si substrate ($N_A \sim 10^{15}$ cm$^{-3}$, Boron) using e-beam evaporation, as illustrated in Fig. 4a. Second, optical lithography, employing a laser-writer from Microtech, delineates the pattern in $SiO_2$, which is then

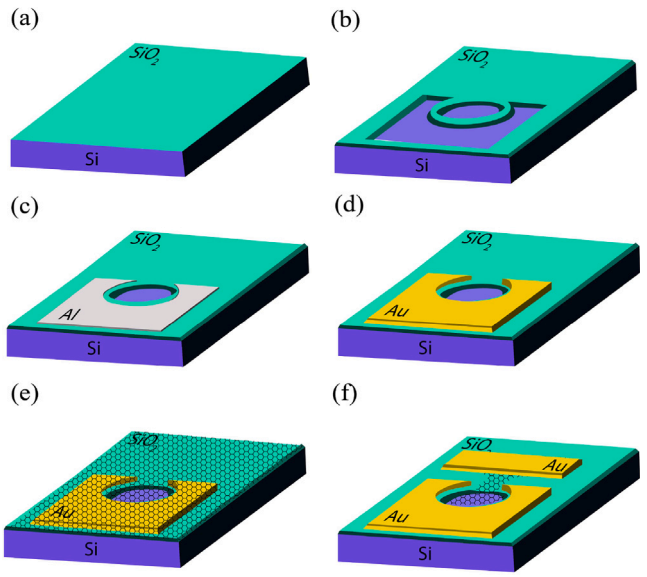


**Fig. 4.** The process of creating Si-Single Layer Graphene (SLG) Schottky: (a) Deposition of a SiO2 layer, (b) Defining areas for Schottky and Ohmic contacts, (c) Forming Al Ohmic contacts, (d) Depositing an Au protection layer, (e) Transferring SLG, (f) Shaping the SLG, (g) Depositing Au contacts onto SLG, and (h) Depositing an Au back mirror. Retrieved from [27].

etched in a BOE solution; as it can be seen in Fig. 4b. Third, Al/Cr/Au (50nm/3nm/50 nm) three-layer electrodes are fabricated on the p-type Si using evaporation, lithography, and lift-off processes. Before depositing Cr/Au, the Al contacts undergo annealing at 460 °C in $N_2$ to impart them with ohmic behavior; as depicted in Fig. 4c and 4d. Fourth, CVD graphene (0.35 nm) is wet-transferred to the target chips, as shown in Fig. 4e. Subsequently, graphene was patterned using lithography and plasma oxygen etching to create the active graphene/p-Si circular junction with an area of $A = \pi \times 10^{-4}$ $cm^2$, along with a PAD where Cr/Au (3 nm/50 nm) contacts were deposited on graphene via photolithography, evaporation, and lift-off processes; as evidenced in Fig. 4f.

The Raman analysis performed on the graphene layer after the fabrication process revealed a doping level of $9 \times 10^{12}$ $cm^{-2}$ (290 meV), single-layer behavior, and a uniform distribution within the active circular area, as reported in detail in [27].

An optical microscope image of the fabricated device, along with the corresponding Raman spectrum of graphene, is provided in Appendix B as Fig. B.1.

## 3. Results and discussion

### *3.1. Quantum mechanical simulations — band structure and physical parameters – QATK*

The simulations at the quantum mechanical level were conducted to determine the impact of the atomic distance of the graphene–Si interface on the electronic properties of the supercell. The characteristics of the optimized crystal configuration are identified, and the changes caused by the displacement of the graphene layer are analyzed. Moreover, by employing DFT plane-wave simulations, the band structure, effective mass, and work function are calculated in every simulation for a quantitative and qualitative comparison.

For the optimized configuration (see Section 2.1), exhibited in Fig. 2, the graphene sheet was placed 3.4 Å away from the Si crystal. This interlayer distance is consistent with the value reported by Sun et al. in their DFT study on graphene transferred on Si(110), where weak van der Waals interactions dominate the interface [48]. The band structure obtained for this configuration is displayed in Fig. 5(a). The conduction and valence bands are close to each other, resulting in the absence of a band gap. Consequently, the interface acts as a metal since electrons can move freely from the valence to the conduction band.

Next, the graphene layer was displaced by −1 Å, positioning it at a distance of 2.4 Å from the Si crystal. The band structure in Fig. 5(b) indicates that, in this configuration, the metallic properties of the interface have intensified. The conduction and valence bands are closer together and more flattened, allowing electrons to move more freely between bands, resulting in enhanced direct conduction. Additionally, as shown in Table 2, the effective mass has decreased. Due to the inverse relationship between effective mass and conductivity, this suggests an increase in the latter, further reinforcing the earlier conclusion.

Subsequently, the graphene sheet was displaced by +2.5 Å from the optimized configuration, placing it 5.9 Å away from the Si crystal. In this case, the band structure in Fig. 5(c) reveals a shift in the interface properties, with a small indirect band gap emerging between the conduction and valence bands in the $V \rightarrow U$ path, indicating a reduction in metallic behavior. As a result, electron movement between bands is more restricted. Moreover, as exhibited in Table 2, the effective mass has increased. Again, considering the inverse relationship between effective mass and conductivity, this suggests a decrease in the latter, which aligns with the previous observation.

In addition, the band structure of pristine graphene is shown in Fig. 5(d) as a reference to illustrate the modifications produced by the interaction between the C atoms and the Si substrate. The calculated band structure exhibits a well-defined Dirac point at the Fermi level, where the conduction and valence bands meet, resulting in the characteristic negligible band gap expected for semimetallic systems. Near this crossing point, the bands display linear dispersion, forming a Dirac cone [49]. Remarkably, the conduction and valence bands near the Fermi level exhibit high symmetry. These characteristics underscore graphene's exceptional electronic properties, including its high electron mobility. In contrast, the band structure of the optimized graphene–Si interface shown in Fig. 5(a) reveals substantial differences. The Dirac cone is no longer preserved, and multiple extra bands appear near the Fermi level. This disappearance of the Dirac point, along with the emergence of additional states, indicates strong hybridization between graphene and silicon electronic states [50]. These changes clearly demonstrate the impact of silicon interactions on the intrinsic properties of graphene.

Notably, regarding the quantitative results, [51] reports a work function of 4.5 eV for pristine graphene. In this study, the work function obtained for the optimized configuration closely aligns with the value of 4.79 eV measured in [27]. The increase in the work function of 290 meV compared to pristine graphene is attributed to charge transfer at the graphene-p-type Si interface. When Si and graphene come into contact, electrons transfer from Si to graphene to reach equilibrium, effectively raising graphene's work function [52,53]. At a separation of 3.4 Å , this interaction is strong enough to induce an electrostatic potential shift in graphene, further increasing the energy required to extract an electron, which is reflected as a higher work function [53].

Furthermore, when graphene is closer to Si, the work function decreases, indicating a stronger interaction with the p-type silicon and increased charge transfer. This transfer shifts the Fermi level of graphene upward, resulting in a reduced work function. On the other hand, when graphene is farther from silicon, the work function increases. This suggests a weaker interaction, leading to less charge transfer and a higher work function for graphene, with its Fermi level moving downward.

To summarize, the effects of displacing the graphene sheet are reflected in the changes in work function and effective mass. When the graphene sheet is closer to the silicon crystal, both the work function and effective mass decrease. Contrary to this, when the graphene sheet is farther from the silicon crystal, these values increase. This demonstrates that the electronic properties are strongly influenced by the geometrical parameters, as shown in the results in Table 2.

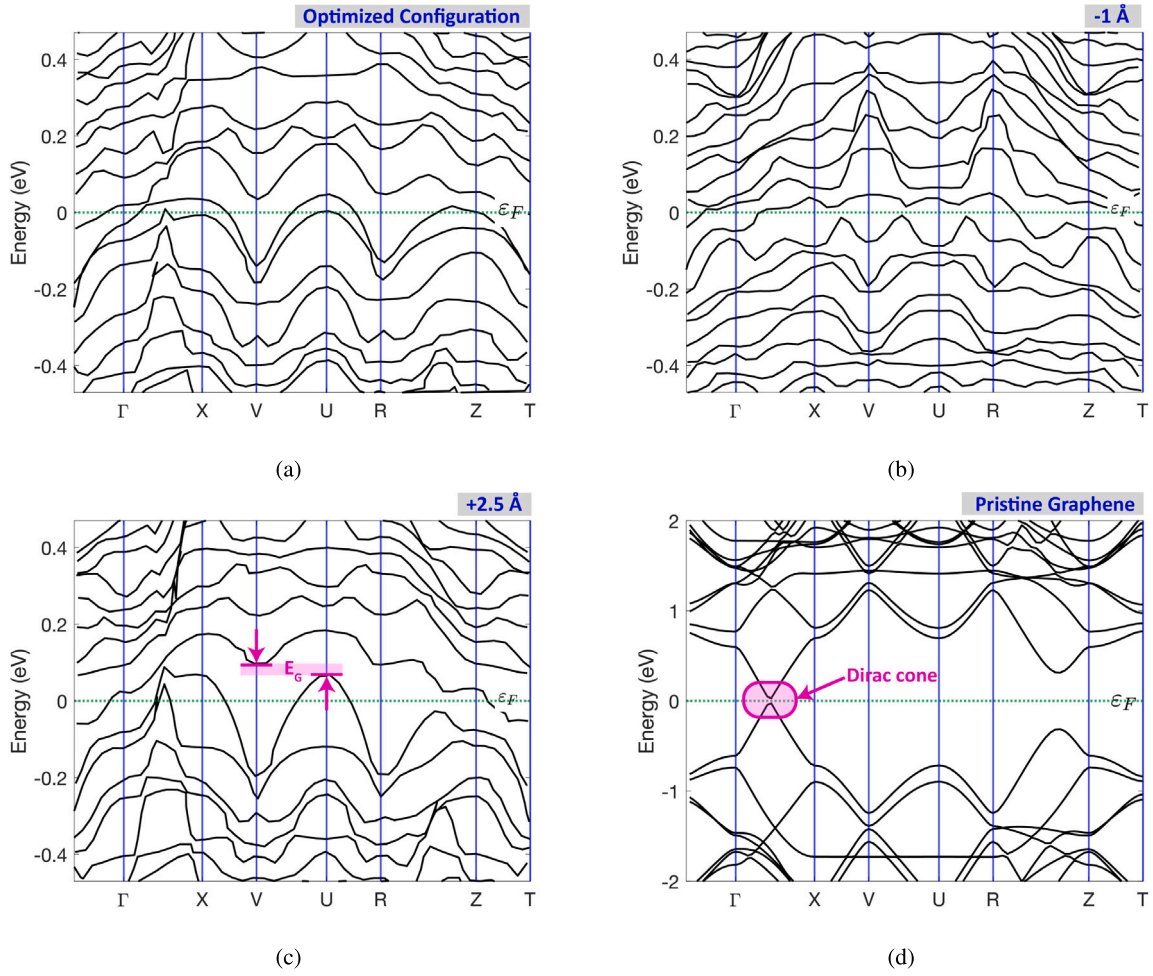


**Fig. 5.** Band structures of: (a) Graphene–Si interface at the optimized configuration, (b) Graphene sheet displaced by −1 Å, (c) Graphene sheet displaced by +2.5 Å, and (d) Pristine graphene. The Fermi level is represented by $\varepsilon_F$ (green dotted line).

**Table 2**
Physical parameters.

| Configuration | Work function (eV) | Effective mass ($m^*$) |
|---|---|---|
| Pristine Graphene | 4.5 | – |
| Optimized | 4.781765 | 0.859 |
| −1 Å | 4.615097 | 0.187 |
| +2.5 Å | 4.815251 | 0.882 |

### 3.2. Finite elements simulations — Sentaurus

To model the graphene/p-Si diode at the device level, it was important first to determine the current transport mechanisms at the interface. According to (1), the recombination velocity $v_{rh}$ plays a crucial role in determining how the current is transported. Therefore, an initial set of simulations was conducted in Sentaurus varying $v_{rh}$ from $10^2$ to $2 \times 10^6$ cm/s. Fig. 6 presents the four most relevant J–V curves at different values of $v_{rh}$.

For a low $v_{rh}$ of $10^2$ and $10^3$ cm/s, the dominant mechanism is thermionic emission. When measuring the subthreshold swing $SS$ for the first curve, a value of 71.3 mV/dec was obtained along with an ideality factor $\eta = 1$, which is very close to the standard value of 60 mV/dec (pure thermionic emission). Similarly, for the second curve, $SS$ was measured at 151.8 mV/dec and $\eta = 2$, indicating a deviation from the standard value, though thermionic emission still dominates over diffusion. This can be further confirmed by the drift velocity calculated in Sentaurus as $v_D = 2.16 \times 10^5$ cm/s; since in both cases $v_{rh} \ll v_D$, thermionic emission remains the governing mechanism, and the saturation current density $J_{TED}$ equals $J_{TE}$ (see (1)).

Conversely, when $v_{rh}$ is high, at $1 \times 10^6$ cm/s and $2 \times 10^6$ cm/s, the current transport is dominated by diffusion rather than thermionic emission. In these cases, since $v_{rh} \gg v_D$, the diffusion process becomes the limiting factor, and the saturation current density $J_{TED}$ equals $J_D$ (see (1)). Here, the $SS$ values were also calculated, yielding 664.0 mV/dec and 672.8 mV/dec, respectively, and $\eta = 11$ for both cases, which is significantly higher than the standard value.

With this initial set of simulations, it was determined that the forward bias curve was significantly affected by series resistance. As a result, a first range was established for the J–V calibration in this work [−2 V to −0.4 V]. Series resistance bends and distorts the characteristic J–V curve. To mitigate this effect, the compact model described in (2) was implemented. Both the original curve with series resistance and that with the compact model are depicted in Fig. 6. From this point forward, only the curves using the compact model will be considered.

Fig. 6 also shows that varying $v_{rh}$ affects the magnitude of the subthreshold and reverse current density [−0.4 V to 10 V]. For lower values of $v_{rh} = 10^2$ and $10^3$ cm/s, the current density is lower since the recombination velocity is insufficient to drive significant carrier transport. On the contrary, for higher values of $v_{rh} = 1 \times 10^6$ and $2 \times 10^6$ cm/s, the current density is higher because the increased recombination velocity enhances the carrier diffusion across the interface, leading to greater injection of charge carriers and higher current flow.

Next, it was necessary to study and characterize the remaining transport phenomena dominating the subthreshold and reverse bias

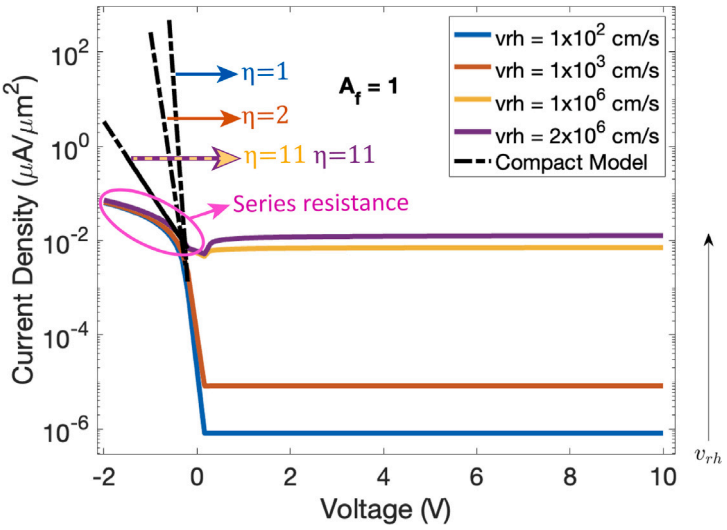


**Fig. 6.** J–V curves without (curves enclosed in the pink circle) and with (black dashed curves) the compact model, varying $v_{rh}$: $1 \times 10^2$ cm/s (blue), $1 \times 10^3$ cm/s (red), $1 \times 10^6$ cm/s (yellow), $2 \times 10^6$ cm/s (purple). $A_f$ stands for Area factor.

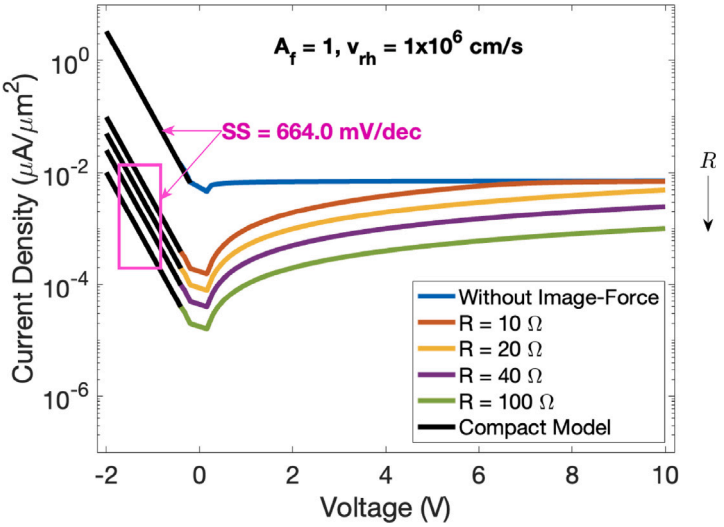


**Fig. 7.** J–V curves without (blue curve) and with (other curves) image-force lowering, varying $R$: 10 Ω (red), 20 Ω (yellow), 40 Ω (purple), 100 Ω (green), and for given $A_f$ and $v_{rh}$.

regions. Thus, a second range for subthreshold and reverse bias [−0.4 V to 10 V] was established for the J–V calibration. In this range, the Sentaurus model for image-force lowering was further explored by varying the interface resistance ($R$) from 10 Ω to 100 Ω. A value of $v_{rh} = 1 \times 10^6$ cm/s was considered.

Fig. 7 exhibits a comparison between the J–V curve without the image-force lowering effect and four J–V curves that include image-force lowering at different values of $R$. The figure illustrates that image-force lowering significantly impacts the magnitude of the reverse current. In Schottky diodes, image-force lowering reduces the effective barrier height at the metal–semiconductor interface [46]. Since this effect is more pronounced under reverse bias conditions [46], a focused effort was made to accurately describe this phenomenon in said voltage range.

When comparing the curves without image-force lowering to those with the effect and varying interface resistances, through Fig. 7, it becomes evident that image-force lowering shifts the entire curve downward. Although the $SS$ remains unchanged, the current density decreases significantly, by two to three orders of magnitude, depending on the value of the resistance at the metal–semiconductor interface $R$. This behavior highlights the critical role of $R$ in limiting charge transport across the junction, despite the reduced Schottky barrier height caused by image-force lowering.

Moreover, it was established that $R$ also affects the electric field distribution at the junction [54,55]. Higher interface resistances, i.e., $R = 40, 100$ Ω, lead to a reduced electric field, which weakens the image-force lowering effect. This makes the Schottky barrier more difficult to surpass, decreasing the reverse current density. Conversely, lower values of $R$, i.e., $10, 20$ Ω, maintain a stronger electric field, which, in turn, increases the image-force lowering effect. This causes the Schottky barrier to be easier to surpass, increasing the reverse current density. Therefore, these results also highlight the existing dependence between the Schottky barrier height $\Phi_B$ and the reverse bias voltage. Thus, the resistance at the junction influences the electric field distribution, affecting the image-force lowering effect. Lower resistance strengthens the electric field, enhancing the image-force lowering effect and making it easier for electrons to overcome the barrier. Higher resistance weakens the field, reducing this effect and making it harder to surpass the barrier

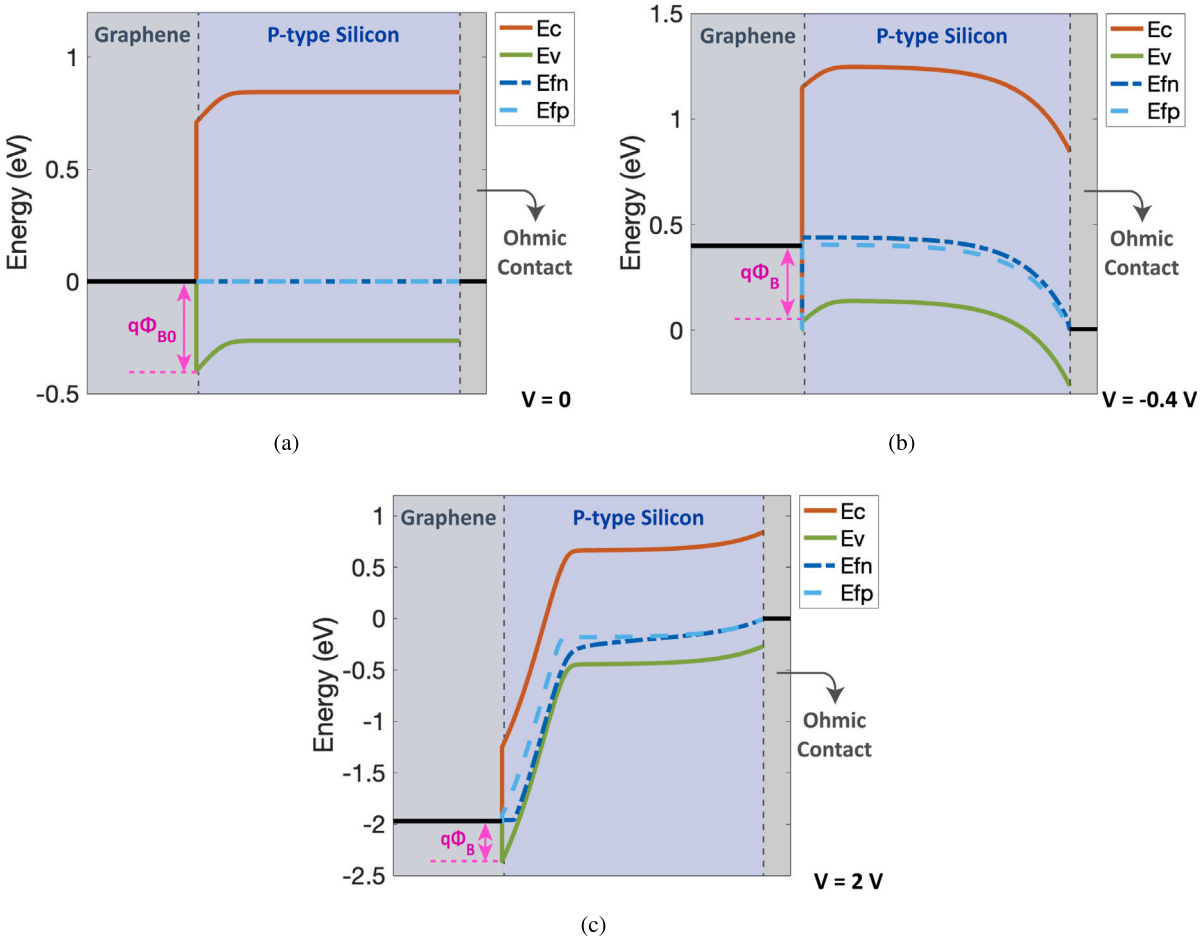


**Fig. 8.** Band Diagrams — Schottky Barrier Modulation: (a) at Equilibrium ($V = 0$), (b) under Forward Bias ($V = -0.4$ V), and (c) under Reverse Bias ($V = 2$ V). The conduction band (orange curve), valence band (green curve), and quasi-Fermi levels for electrons and holes (blue and light blue dotted curves) are displayed.

Furthermore, since image-force lowering induces a bias-dependent modulation of the Schottky barrier height, it is important to analyze the band diagrams at the interface. Fig. 8 exhibits the energy band profiles in equilibrium, forward bias, and reverse bias, effectively demonstrating this effect.

Fig. 8(a) shows the band diagram for the Schottky diode at equilibrium ($V = 0$), where the calculated Schottky barrier height is $|\Phi_{B_0}| = 0.40$ eV. Under forward bias ($V = -0.4$ V), as shown in Fig. 8(b), the barrier height remains approximately $|\Phi_{B_0}| = 0.40$ eV, indicating that $\Delta\Phi_B$ is insignificant in this condition. Conversely, in reverse bias ($V = 2$ V), the band diagram in Fig. 8(c) demonstrates a reduction in the Schottky barrier height to $|\Phi_{B_0}| = 0.34$ eV. This underscores the pronounced effect of image-force lowering in reverse bias, where $\Delta\Phi_B \approx 60$ meV becomes relevant, making Schottky barrier modulation non-negligible.

Finally, Table 3 summarizes the results of the finite element simulation and the main driving physical parameters, $v_{rh}$ and $R$. It highlights the mechanisms influenced by these parameters, including thermionic emission, diffusion, and the image-force lowering effect. The table details the specific impacts of $v_{rh}$ and $R$ on the J–V curve, such as shifts in current density, variations in the subthreshold swing ($SS$), and modulation of the Schottky barrier height ($\Phi_B$). Moreover, it identifies the voltage ranges where each parameter has the greatest impact, providing critical insights into the transport mechanisms at the graphene/p-Si interface.

These results are the highlight of this work, as they provide a comprehensive subthreshold and reverse bias model applicable to any graphene–Si Schottky device. In the following section, this model is applied to an experimental case to determine the parameters that best fit the behavior of a photodetector device and to validate the theoretical findings with practical observations.

Note, when activating the tunneling effect in Sentaurus, it was observed that it does not significantly impact the J–V curve, as no changes in the results were detected. This is primarily attributed to the device dimensions detailed in Table 1. According to [56,57], tunneling is minimal in devices where the thickness of one material is substantially large. In this case, the silicon layer is considerably thicker than the graphene layer, making significant hole tunneling unlikely. A more detailed discussion of the tunneling effect is provided in Appendix C.

### 3.3. Comparison with experimental results

In order to validate the developed subthreshold and reverse bias model, the simulations conducted on the device depicted in Figs. 6 and 7 are calibrated and compared with the experimental data from [27].

When comparing the simulation results in forward bias ([−2 V to −0.4 V]) to the experimental curve, it was determined that, at the interface of the photodetector device (PD), the current density is best described by the thermionic-emission–diffusion theory, with diffusion dominating over thermionic emission. The experimental $SS$ reported in [27] corresponds to $SS = 664.9$ mV/dec and $\eta = 11$. This also suggests that the recombination velocity in the PD is high, in the order of $10^6$ cm/s. Therefore, from Fig. 6, the simulation that best fits the experimental curve is the one where $v_{rh} = 1 \times 10^6$ cm/s and $SS = 664.0$ mV/dec.

Similarly, when comparing the simulation results in the second range to the experimental curve, it was found that, at the junction

**Table 3**
Summary of the main driving physical parameters finite elements simulation.

| Parameter | Mechanism | Effect on J–V curve | Voltage range |
|---|---|---|---|
| $v_{rh}$ | Thermionic Emission-Diffusion | Variation of $SS$ | Forward bias |
| | | Shifts the magnitude of current density | Subthreshold and Reverse bias |
| $R$ | Image-Force-Lowering | Reduces the magnitude of current density | Entire range |
| | | Modulates $\Phi_B$ | Graphene/p-Si interface |

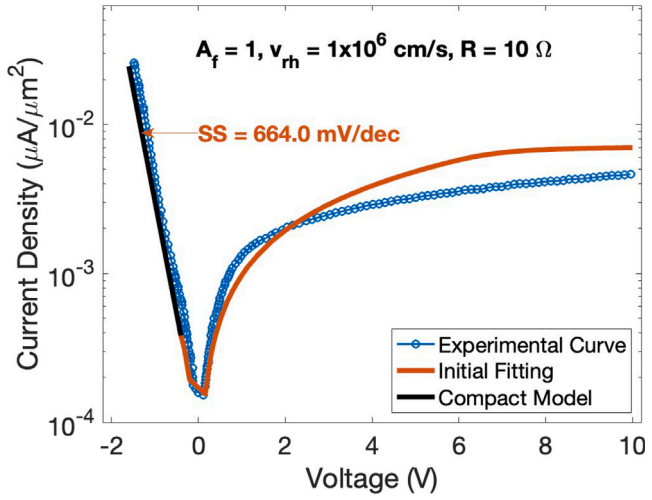


**Fig. 9.** Comparison with experimental results: J–V curves initial fitting for given $A_f$, $v_{rh}$, and $R$.

of the PD, the image-force lowering effect has a significant impact on determining the reverse current density magnitude. The results presented in [27] suggest that the PD's interface resistance has a low value, which strengthens the image-force lowering effect and increases reverse current density. From Fig. 7, curves with lower resistance values fit the experimental data better, with the best fit achieved by the curve with a resistance of 10 Ω.

Fig. 9 exhibits the first fitting performed for the experimental curve according to the observations compiled before, i.e., $v_{rh} = 1 \times 10^6$ cm/s and $R = 10$ Ω with image-force lowering. From this figure, it is evident that after the initial fitting, a re-calibration of $v_{rh}$ was necessary solely to achieve a better correspondence to the experimental data. For this, a new simulation was run for $v_{rh}$ values between $3\times10^5$ and $1\times10^6$ cm/s, and $R = 10$ Ω with image-force lowering. As shown in Fig. 10, the best fit occurs with a value of $v_{rh} = 5 \times 10^5$ cm/s. In this case, since $v_{rh}$ is still greater than $v_D$, it can be concluded that the diffusion transport mechanism continues to dominate over thermionic emission.

Additionally, it was observed that when applying the image-force lowering model, for values of $v_{rh} \geq 9 \times 10^5$ cm/s, the reverse current density shows signs of saturation, indicating that further increases in $v_{rh}$ do not significantly affect the current transport. This suggests that beyond this threshold, the impact of diffusion-driven transport is maximized, and additional velocity does not enhance carrier injection.

In summary, Fig. 11 combines the best fits from both ranges ([−2V to −0.4V] and [−0.4 V to 10V]). The final Subthreshold and Reverse Bias models are depicted, along with the Compact model (in forward bias) for the entire range [−2V to 10V]. Table 4 summarizes the final parameters of the Subthreshold and Reverse Bias model. Notably, the key parameters of the subthreshold model that influence the diode current—$V_{rh}$, $SS$, $\eta$, and $\Phi_{B_0}$—closely align with those found in [27]. It is important to mention that the value of $\Phi_{B_0}$ was extracted from Fig. 8(a).

**Table 4**
Final model parameters.

| Parameter | This work | [27] |
|---|---|---|
| $v_{rh}$ | $5 \times 10^5$ cm/s | – |
| $R$ | 10 Ω | – |
| $SS$ | 664.0 mV/decade | 664.9 mV/decade |
| $\eta$ | 11 | 11 |
| $\phi_{B_0}$ | 0.40 eV | 0.46 eV |

## 4. Conclusions

In this paper, a novel approach was employed to thoroughly study and model the graphene–Si interface. In the quantum-mechanical analysis, simulations were conducted to understand the electronic properties at the junction and to obtain relevant physical parameters. As shown in Table 2, for the optimized configuration, the work function was found to be 4.78 eV, and the effective mass $m_*$ was 0.589 $m_0$. Likewise, through the band structure diagrams in Fig. 5, it was determined how the atomic distance between graphene and Si impacts the electronic properties of the interface.

Subsequently, the physical parameters acquired were employed in the finite-element simulations. A subthreshold and reverse bias TCAD-based model was developed in Sentaurus by studying the physical phenomena at the graphene/p-Si interface that define the J–V curve. Both thermionic emission–diffusion and image-force lowering mechanisms were analyzed, and the main conclusions are summarized in Table 3. Overall, when $v_{rh} \ll v_D$, thermionic emission dominates the current transport process, while when $v_{rh} \gg v_D$, diffusion becomes the dominating mechanism. Additionally, it was concluded that image-force lowering is a significant factor that influences current density and explains the existing dependency between $\Phi_B$ and the applied bias, as evidenced in Fig. 8.

Finally, the derived model was compared with experimental data from the PDs in [27]. Since a higher $SS$ and reverse current are necessary for this application, the final parameters established are shown in Table 4. These results aligned with those from [27], demonstrating consistency from the atomic level to the device level and bridging theory, simulation, and practical implementation. The novelty of this work lies in the comprehensive, multi-scale methodology that integrates quantum-mechanical analysis, device simulation, and experimental validation within a single framework. This approach provides a robust foundation for future research and development, enabling a more precise and predictive characterization of graphene–Si interfaces in various semiconductor applications. Notably, while this study focuses on graphene-based junctions with p-type silicon, the proposed framework is broadly applicable to similar junctions across different semiconductor types, fabrication methods, and experimental setups.

The importance of this TCAD model for Schottky diodes with graphene–Si interfaces extends beyond photodetectors, including applications in energy-harvesting devices, sensors, and other advanced technologies. By combining quantum-mechanical and device simulations, the model enables the adjustment of key design parameters such as the J–V curve, subthreshold swing, current density, and Schottky

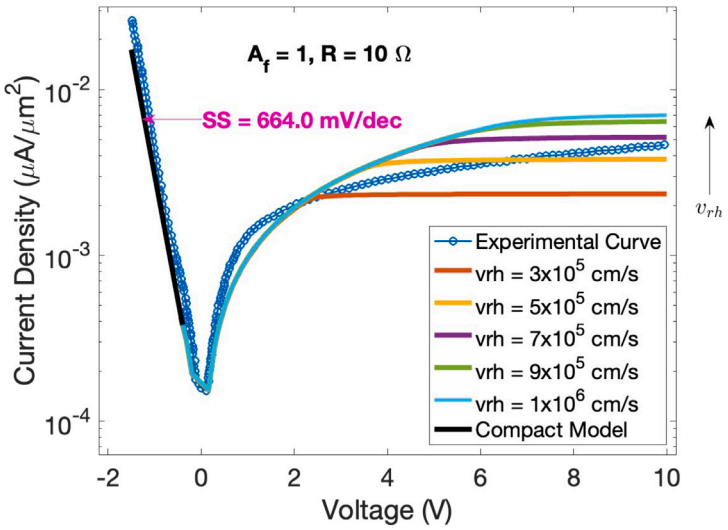


**Fig. 10.** Comparison with experimental results: J–V curves with $v_{rh}$ re-calibration: $3 \times 10^5$ cm/s (red), $5 \times 10^5$ cm/s (yellow), $7 \times 10^5$ cm/s (purple), $9 \times 10^5$ cm/s (green), $1 \times 10^6$ cm/s (light blue), and for given $A_f$ and $R$.

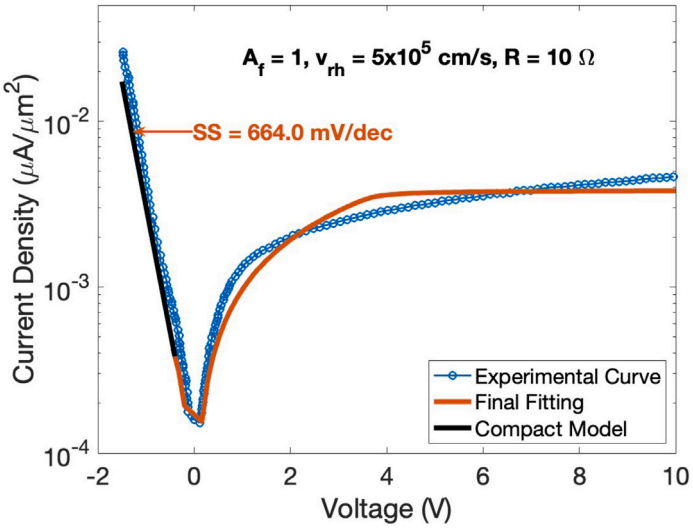


**Fig. 11.** Comparison with experimental results: J–V curves best and final fitting for given $A_f$, $v_{rh}$, and $R$.

barrier height. This understanding allows researchers and engineers to optimize device performance to meet specific application requirements. For example, maximizing photocurrent in solar cells or improving sensitivity and speed in photodetectors can be achieved through informed tuning of barrier height and interface quality. Additionally, the model allows simulations under various operating conditions, providing valuable insights that closely align with experimental observations.

## CRediT authorship contribution statement

**Katty Beltrán:** Writing – original draft, Validation, Software, Investigation, Data curation. **Jhon Paredes:** Validation, Software, Methodology, Investigation, Formal analysis, Data curation. **F. Javier Torres:** Writing – original draft, Validation, Supervision, Software, Formal analysis. **Alfredo Sánchez:** Writing – original draft, Supervision, Software, Methodology, Investigation, Formal analysis. **César Zambrano:** Supervision, Software, Methodology, Investigation. **Maurizio Casalino:** Methodology, Investigation, Formal analysis, Conceptualization. **Paul Prócel:** Validation, Supervision, Software, Methodology, Investigation, Formal analysis, Conceptualization. **Olindo Isabella:** Methodology, Formal analysis. **Luis Miguel Prócel:** Validation, Supervision, Software, Project administration, Methodology, Investigation, Formal analysis, Data curation, Conceptualization.

## Declaration of competing interest

The authors declare that they have no known competing financial interests or personal relationships that could have appeared to influence the work reported in this paper.

## Acknowledgments

We extend our gratitude to Synopsys Chile for the invaluable support provided to USFQ in the use of their entire platform of design and simulation tools. Their support has been crucial for the development of our research and academic projects. Synopsys Chile's support and commitment to fostering innovation in scientific research are truly appreciated.

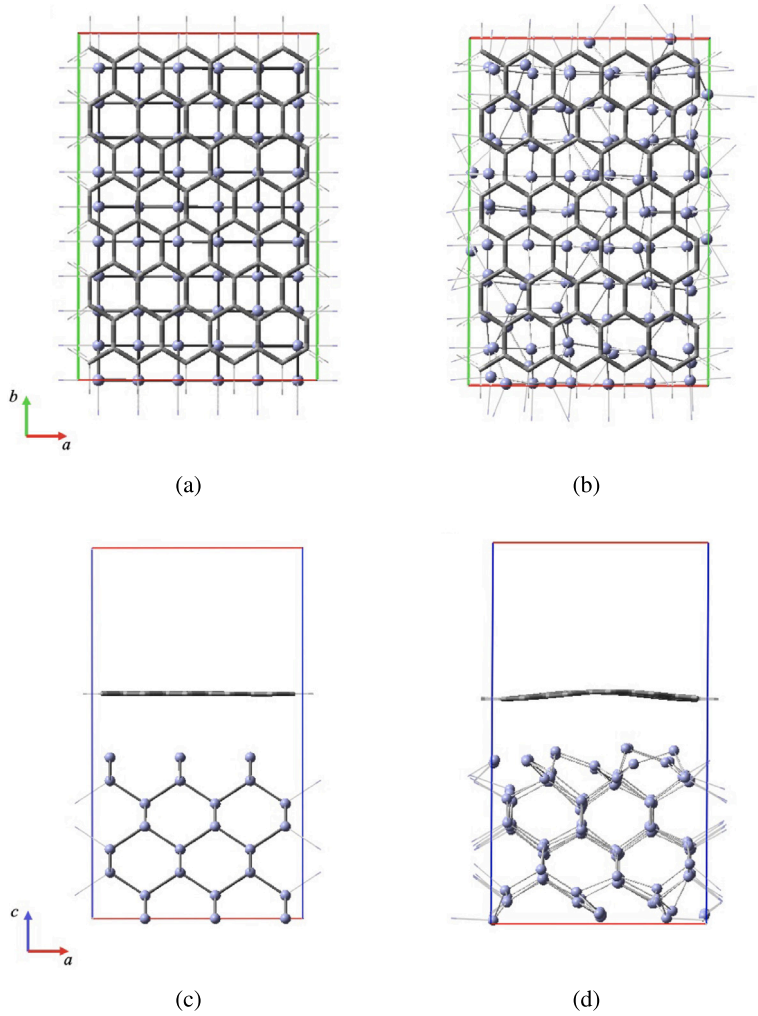


**Fig. A.1.** View of the *ab* (top) and *ac* (bottom) planes of the unit cell at the Si/C interface before (a, c) and after (b, d) geometric optimization at the PBE level of theory. Carbon and silicon atoms are shown in gray and purple, respectively.

## Appendix A. Geometrical optimization of the Si/C interface - quantum mechanical calculations

The Si/C interface before and after geometric optimization at the PBE level of theory is presented in Fig. A.1.

## Appendix B. Optical microscope image and Raman spectrum of graphene — experimental case study

An optical microscope image of the fabricated device is shown in Fig. B.1(a). In addition, Fig. B.1(b) presents Raman spectra of graphene at different stages: on copper (Cu) (green curve), after transfer to Si (black curve), and following device fabrication (blue), each with appropriate silicon background subtraction. Raman measurements were performed using a Renishaw InVia microscope equipped with a 100× objective lens and a 514.5 nm excitation wavelength.

On Cu, the spectrum displays prominent G and 2D peaks, with a negligible D peak, indicating high-quality monolayer graphene. The 2D peak is a single Lorentzian centered at ~2712 $cm^{-1}$ (FWHM ~ 29 $cm^{-1}$), while the G peak appears at ~ 1595 $cm^{-1}$ (FWHM ~ 9.5 $cm^{-1}$). Intensity and area ratios are $I(2D)/I(G) \approx 1.9$ and $A(2D)/A(G) \approx 5.8$.

After transfer to Si, the 2D peak remains Lorentzian (Pos ~2691 $cm^{-1}$, FWHM ~ 35 $cm^{-1}$). The G peak shifts to ~1587.5 $cm^{-1}$ (FWHM ~ 19.6 $cm^{-1}$), with increased ratios: $I(2D)/I(G) \approx 4.32$ and $A(2D)/A(G) \approx 7.16$, consistent with p-type doping (~$2.4 \times 10^{12}$ $cm^{-2}$, ~200 meV).

Following device fabrication, the G and 2D peaks are located at ~1592.4 $cm^{-1}$ (FWHM ~ 10.7 $cm^{-1}$) and ~2691.4 $cm^{-1}$ (FWHM ~ 31.1 $cm^{-1}$), respectively. The corresponding intensity and area ratios are $I(2D)/I(G) \approx 2.53$ and $A(2D)/A(G) \approx 6.3$, suggesting increased doping (~$9 \times 10^{12}$ $cm^{-2}$, ~290 meV). A measurable D peak emerges, with $I(D)/I(G) \approx 0.14$, indicating some defect introduction during processing.

## Appendix C. Tunnel effect — finite elements simulations

The following finite element simulations were performed using Sentaurus, where the band-to-band nonlocal tunneling model was enabled to assess whether the spatial extent of the tunneling process significantly influences the current density and contributes to the overall J–V characteristics. For this, a parametric sweep of the tunneling path length, denoted as $L_t$, was carried out. By default, Sentaurus uses the WKB (Wentzel–Kramers–Brillouin) approximation to calculate the tunneling probability, which is then used to determine the tunneling current $J_t$. Further details on the corresponding models and equations are available in the Sentaurus Device manual (see [47]).

Fig. C.1 compares the J–V curves with and without the tunneling effect, for a recombination velocity of $v_{rh} = 1 \times 10^6$ cm/s, considering both the presence and absence of the image-force-lowering effect.

First, the tunneling effect was analyzed independently by varying the tunneling length $L_t$ across values of 1 nm, 10 nm, 100 nm, and 1 μm. As seen in Fig. C.1, the J–V curves obtained for all $J_t$ values

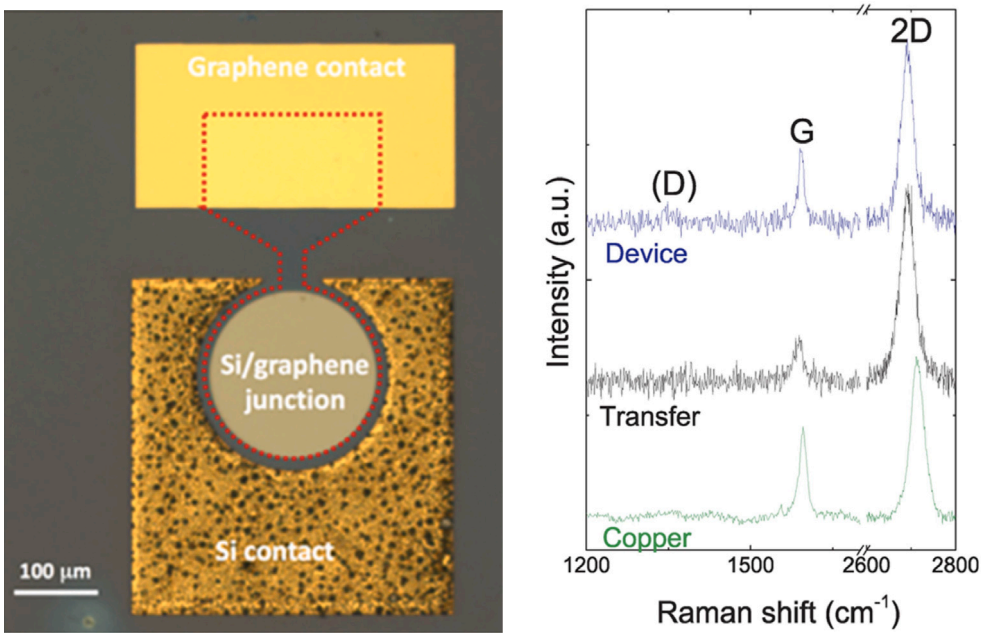


(a) (b)

**Fig. B.1.** (a) Microscope image of the device to which the results of this work refer. (b) Raman spectra, with the silicon substrate contribution subtracted, of graphene in three different conditions: (green) as-grown on copper, (black) transferred onto Si, and (blue) on Si after the fabrication process. Reprinted (adapted) with permission from Casalino, M.; Sassi, U.; Goykhman, I.; Eiden, A.; Lidorikis, E.; Milana, S.; De Fazio, D.; Tomarchio, F.; Iodice, M.; Coppola, G.; Ferrari, A.C. Vertically Illuminated, Resonant Cavity Enhanced, Graphene–Silicon Schottky Photodetectors. ACS Nano 2017, 11, 10955-10963. Copyright 2017 American Chemical Society.

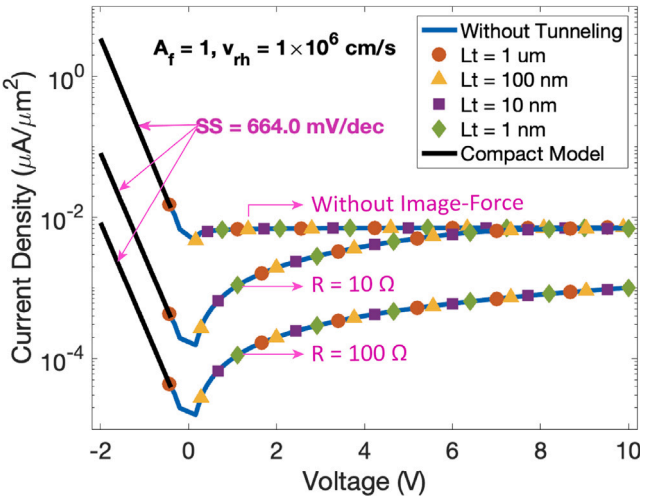


**Fig. C.1.** J–V curves without (blue curve) and with (other curves) tunneling effect, varying $L_t$: 1 µm (red circle), 100 nm (yellow traingle), 10 nm (purple square), 1 nm (green diamond), and for given $A_f$ and $v_{rh}$.

were exactly the same as the one without tunneling, indicating that the tunneling process does not contribute significantly under these conditions.

Subsequently, tunneling was re-evaluated in the presence of the image-force-lowering effect for interface resistances of $R = 10\ \Omega$ and $100\ \Omega$, representing the lower and upper bounds discussed in Section 3.2. Once again, the J–V curves with tunneling (at all $L_t$ values) were found to be identical to those without tunneling, confirming that the tunneling current has no meaningful influence on the overall current density in either case.

These results show that the tunneling effect is minimal in devices where one of the materials is significantly thicker [56,57]. In this graphene–silicon Schottky diode, although the graphene is only 0.35 nm thick, the silicon layer measures 200 µm (approximately 500,000 times thicker) making the tunneling probability extremely low. In addition, another important factor influencing tunneling is the width of the depletion region at the silicon side of the interface, which acts as the effective tunneling barrier [56]. This directly determines the likelihood of carriers tunneling across the junction, and its value depends mainly on the doping concentration and built-in potential [44].

Since the silicon is lightly p-doped with a boron concentration of $N_A = 10^{15}\ \text{cm}^{-3}$, the depletion width on the silicon side is relatively large (in the range hundreds of nanometers). A wider barrier means a lower probability of quantum-mechanical tunneling, as the tunneling current decreases exponentially with increasing barrier width. It is well known in semiconductor physics, that tunneling becomes relevant only when the doping level is very high (above $10^{18}\ \text{cm}^{-3}$), since this significantly reduces the depletion width to just a few nanometers [44].

In summary, the results from Fig. C.1 show three main curves unaffected by the tunneling effect—one without image-force lowering, and the other two including image-force lowering for different values of interface resistance (10 and 100 Ω). This confirms that other charge transport mechanisms, such as thermionic emission, diffusion, and image-force barrier lowering, dominate over tunneling in this lightly doped graphene–silicon Schottky junction. Therefore, the tunneling effect is considered negligible in this configuration.

It is important to note that silicon–graphene Schottky diodes typically use bulk silicon substrates with thicknesses around a couple hundred µm, which further suppresses tunneling due to the dimensions involved in these types of devices.

## References

[1] C.-C. Chen, M. Aykol, C.-C. Chang, A.F.J. Levi, S.B. Cronin, Graphene-silicon Schottky diodes, Nano Lett. 11 (5) (2011) 1863–1867, http://dx.doi.org/10.1021/nl104364c.

[2] X. Kong, L. Zhang, B. Liu, H. Gao, Y. Zhang, H. Yan, X. Song, Graphene/Si Schottky solar cells: a review of recent advances and prospects, RSC Adv. 9 (2019) 863–877, http://dx.doi.org/10.1039/C8RA08035F.

[3] Y. Ye, L. Dai, Graphene-based Schottky junction solar cells, J. Mater. Chem. 22 (2012) 24224–24229, http://dx.doi.org/10.1039/C2JM33809B.

[4] A.R. Urade, I. Lahiri, K.S. Suresh, Graphene properties, synthesis and applications: A review, JOM 75 (2022) 614–630, http://dx.doi.org/10.1007/s11837-022-05505-8.

[5] B.K. Sharma, J.-H. Ahn, Graphene based field effect transistors: Efforts made towards flexible electronics, Solid-State Electron. 89 (2013) 177–188, http://dx.doi.org/10.1016/j.sse.2013.08.007.

[6] X. Li, Y. Zhu, W. Cai, M. Borysiak, B. Han, D. Chen, R.D. Piner, L. Colombo, R.S. Ruoff, Transfer of large-area graphene films for high-performance transparent conductive electrodes, Nano Lett. 9 (2009) 4359–4363, http://dx.doi.org/10.1021/nl902623y.

[7] W. Liu, L. Li, H. Guo, A. Qadir, S.C. Bodepudi, K. Shehzad, W. Chen, Y.-H. Xie, X. Wang, B. Yu, Y. Xu, Approaching the collection limit in hot electron transistors with ambipolar hot carrier transport, ACS Nano 13 (12) (2019) 14191–14197, http://dx.doi.org/10.1021/acsnano.9b07020, pMID: 31755701.

[8] S.M. Young, C.L. Kane, Dirac semimetals in two dimensions, Phys. Rev. Lett. 115 (2015) 126803, http://dx.doi.org/10.1103/PhysRevLett.115.126803.

[9] V.B. Mbayachi, E. Ndayiragije, T. Sammani, S. Taj, E.R. Mbuta, A.U. Khan, Graphene synthesis, characterization and its applications: A review, Results Chem. 3 (2021) 100163, http://dx.doi.org/10.1016/j.rechem.2021.100163.

[10] H.-J. Choi, S.-M. Jung, J.-M. Seo, D.W. Chang, L. Dai, J.-B. Baek, Graphene for energy conversion and storage in fuel cells and supercapacitors, Nano Energy 1 (4) (2012) 534–551, http://dx.doi.org/10.1016/j.nanoen.2012.05.001.

[11] Y. Xu, K. Shehzad, S.C. Bodepudi, A. Imran, B. Yu, Graphene/silicon solar energy harvesting devices, in: Graphene for Post-Moore Silicon Optoelectronics, Wiley, 2023, pp. 85–105, http://dx.doi.org/10.1002/9783527841011.ch5.

[12] L. Chen, H. He, H. Yu, Y. Cao, D. Yang, Fabrication and photovoltaic conversion enhancement of graphene/n-Si Schottky barrier solar cells by electrophoretic deposition, Electrochim. Acta 130 (2014) 279–285, http://dx.doi.org/10.1016/j.electacta.2014.03.020.

[13] K. Drozdowska, A. Rehman, J. Smulko, S. Rumyantsev, B. Stonio, A. Krajewska, M. Słowikowski, M. Filipiak, P. Sai, G. Cywiński, Enhanced gas sensing by graphene-silicon Schottky diodes under UV irradiation, Sensors Actuators B 396 (2023) 134586, http://dx.doi.org/10.1016/j.snb.2023.134586.

[14] A. Fattah, S. Khatami, Selective H2S gas sensing with a graphene/n-Si Schottky diode, IEEE Sens. J. 14 (11) (2014) 4104–4108, http://dx.doi.org/10.1109/jsen.2014.2334064.

[15] K. Shehzad, T. Shi, A. Qadir, X. Wan, H. Guo, A. Ali, W. Xuan, H. Xu, Z. Gu, X. Peng, J. Xie, L. Sun, Q. He, Z. Xu, C. Gao, Y.-S. Rim, Y. Dan, T. Hasan, P. Tan, E. Li, W. Yin, Z. Cheng, B. Yu, Y. Xu, J. Luo, X. Duan, Designing an efficient multimode environmental sensor based on graphene–silicon heterojunction, Adv. Mater. Technol. 2 (4) (2017) 1600262, http://dx.doi.org/10.1002/admt.201600262.

[16] J. Wang, X. Mu, M. Sun, T. Mu, Optoelectronic properties and applications of graphene-based hybrid nanomaterials and van der Waals heterostructures, Appl. Mater. Today 16 (2019) 1–20, http://dx.doi.org/10.1016/j.apmt.2019.03.006.

[17] F. Xia, T. Mueller, Y. Lin, A. Valdes-Garcia, P. Avouris, Ultrafast graphene photodetector, Nature Nanotechnology 4 (2009) 839–843, http://dx.doi.org/10.1038/nnano.2009.292.

[18] X. Chen, K. Shehzad, L. Gao, M. Long, H. Guo, S. Qin, X. Wang, F. Wang, Y. Shi, W. Hu, Y. Xu, X. Wang, Graphene hybrid structures for integrated and flexible optoelectronics, Adv. Mater. 32 (27) (2020) 1902039, http://dx.doi.org/10.1002/adma.201902039.

[19] J. Zhou, L. Li, A. Qadir, H. Li, J. Lv, K. Shehzad, X. Xu, L. Liu, F. Tian, W. Liu, L. Chen, L. Yu, X. Su, S.C. Bodepudi, H. Hu, Y. Zhao, B. Yu, X. Wang, Y. Xu, Charge sampling photodetector based on van der Waals heterostructures, Adv. Opt. Mater. 10 (24) (2022) 2201442, http://dx.doi.org/10.1002/adom.202201442.

[20] M. Ali, A. Khaliq, M.A. Anwar, J. Lv, M. Malik, T. Feng, S.C. Bodepudi, H. Guo, K. Shehzad, Z. Li, Y. Dong, W. Liu, H. Hu, Y. Zhao, B. Yu, Y. Xu, Graphene channel electron-multiplying charge-coupled pixel, IEEE Access 11 (2023) 37424–37436, http://dx.doi.org/10.1109/ACCESS.2023.3266339.

[21] A. Bartolomeo, Graphene Schottky diodes: An experimental review of the rectifying graphene/semiconductor heterojunction, Phys. Rep. 606 (2016) 1–58, http://dx.doi.org/10.1016/j.physrep.2015.10.003.

[22] M. Casalino, T. Crisci, L. Moretti, M. Gioffré, M. Iodice, G. Coppola, P. Maccagnani, R. Rizzoli, F. Bonafè, C. Summonte, V. Morandi, Silicon meet graphene for a new family of near-infrared resonant cavity enhanced photodetectors, in: 2020 22nd International Conference on Transparent Optical Networks, ICTON, 2020, pp. 1–4, http://dx.doi.org/10.1109/ICTON51198.2020.9203222.

[23] M. Ali, M.A. Anwar, J. Lv, S.C. Bodepudi, H. Guo, K. Shehzad, Y. Dong, W. Liu, X. Wang, A. Imran, H. Hu, Y. Zhao, B. Yu, Y. Xu, Graphene field-effect-coupled detection of avalanche multiplication in silicon, IEEE Trans. Electron Devices 70 (5) (2023) 2370–2377, http://dx.doi.org/10.1109/TED.2023.3262630.

[24] X. Wan, Y. Xu, H. Guo, K. Shehzad, A. Ali, Y. Liu, J. Yang, D. Dai, C.-T. Lin, L. Liu, H.-C. Cheng, F. Wang, X. Wang, H. Lu, W. Hu, X. Pi, Y. Dan, J. Luo, T. Hasan, X. Duan, X. Li, J. Xu, D. Yang, T. Ren, B. Yu, A self-powered high-performance graphene/silicon ultraviolet photodetector with ultra-shallow junction: breaking the limit of silicon? npj 2D Mater. Appl. 1 (1) (2017/04/11) 4, http://dx.doi.org/10.1038/s41699-017-0008-4.

[25] S. Du, W. Lu, A. Ali, P. Zhao, K. Shehzad, H. Guo, L. Ma, X. Liu, X. Pi, P. Wang, H. Fang, Z. Xu, C. Gao, Y. Dan, P. Tan, H. Wang, C.-T. Lin, J. Yang, S. Dong, Z. Cheng, E. Li, W. Yin, J. Luo, B. Yu, T. Hasan, Y. Xu, W. Hu, X. Duan, A broadband fluorographene photodetector, Adv. Mater. 29 (22) (2017) 1700463, http://dx.doi.org/10.1002/adma.201700463.

[26] Y. Xu, A. Ali, K. Shehzad, N. Meng, M. Xu, Y. Zhang, X. Wang, C. Jin, H. Wang, Y. Guo, Z. Yang, B. Yu, Y. Liu, Q. He, X. Duan, X. Wang, P.-H. Tan, W. Hu, H. Lu, T. Hasan, Solvent-based soft-patterning of graphene lateral heterostructures for broadband high-speed metal–semiconductor–metal photodetectors, Adv. Mater. Technol. 2 (2) (2017) 1600241, http://dx.doi.org/10.1002/admt.201600241.

[27] M. Casalino, U. Sassi, I. Goykhman, A. Eiden, E. Lidorikis, S. Milana, D. De Fazio, F. Tomarchio, M. Iodice, G. Coppola, A.C. Ferrari, Vertically illuminated, resonant cavity enhanced, graphene–silicon Schottky photodetectors, ACS Nano 11 (11) (2017) 10955–10963, http://dx.doi.org/10.1021/acsnano.7b04792.

[28] M.S.N. Alnassar, S. Luong, H.N. Tran, J.G. Partridge, A.S. Holland, Simulation of graphitic contacts to p-type Si using a metal-resistor-semiconductor (M-R-S) model implemented in TCAD, Int. J. Numer. Model. 31 (3) (2018) http://dx.doi.org/10.1002/jnm.2302.

[29] Y. Kuang, Y. Liu, Y. Ma, J. Xu, X. Yang, J. Feng, TCAD analysis of graphene silicon Schottky junction solar cell, in: Z. Zhou (Ed.), International Symposium on Photonics and Optoelectronics 2015, vol. 9656, International Society for Optics and Photonics, SPIE, 2015, p. 96560W, http://dx.doi.org/10.1117/12.2197678.

[30] H.N. Waltenburg, J. Yates, Surface chemistry of silicon, Chem. Rev. 95 (5) (1995) 1589–1673, http://dx.doi.org/10.1021/cr00037a600.

[31] H.-W. Guo, Z. Hu, Z.-B. Liu, J.-G. Tian, Stacking of 2D materials, Adv. Funct. Mater. 31 (4) (2021) 2007810, http://dx.doi.org/10.1002/adfm.202007810.

[32] B. Kiraly, A.J. Mannix, M.C. Hersam, N.P. Guisinger, Graphene–silicon heterostructures at the two-dimensional limit, Chem. Mater. 27 (17) (2015) 6085–6090, http://dx.doi.org/10.1021/acs.chemmater.5b02602.

[33] J.P. Perdew, K. Burke, M. Ernzerhof, Generalized gradient approximation made simple, Phys. Rev. Lett. 77 (18) (1996) 3865–3868, http://dx.doi.org/10.1103/physrevlett.77.3865.

[34] J. Paier, R. Hirschl, M. Marsman, G. Kresse, The Perdew–Burke–Ernzerhof exchange-correlation functional applied to the G2-1 test set using a plane-wave basis set, J. Chem. Phys. 122 (23) (2005) 234102, http://dx.doi.org/10.1063/1.1926272.

[35] G. Kresse, J. Hafner, Ab initio molecular dynamics for liquid metals, Phys. Rev. B 47 (1) (1993) 558–561, http://dx.doi.org/10.1103/PhysRevB.47.558.

[36] G. Kresse, J. Hafner, Ab initio molecular-dynamics simulation of the liquid-metal–amorphous-semiconductor transition in germanium, Phys. Rev. B 49 (20) (1994) 14251–14269, http://dx.doi.org/10.1103/PhysRevB.49.14251.

[37] G. Kresse, J. Furthmüller, Efficiency of ab-initio total energy calculations for metals and semiconductors using a plane-wave basis set, Comput. Mater. Sci. 6 (1) (1996) 15–50, http://dx.doi.org/10.1016/0927-0256(96)00008-0.

[38] G. Kresse, J. Furthmüller, Efficient iterative schemes for ab initio total-energy calculations using a plane-wave basis set, Phys. Rev. B 54 (16) (1996) 11169–11186, http://dx.doi.org/10.1103/PhysRevB.54.11169.

[39] F. Neese, A. Hansen, F. Wennmohs, S. Grimme, Accurate theoretical chemistry with coupled pair models, Acc. Chem. Res. 42 (5) (2009) 641–648, http://dx.doi.org/10.1021/ar800241t.

[40] H. Liu, A.S. Deshmukh, N. Salowitz, J. Zhao, K. Sobolev, Resistivity signature of graphene-based fiber-reinforced composite subjected to mechanical loading, Front. Mater. 9 (2022) http://dx.doi.org/10.3389/fmats.2022.818176.

[41] L.F.C. Pereira, Investigating mechanical properties and thermal conductivity of 2D carbon-based materials by computational experiments, Comput. Mater. Sci. 196 (2021) 110493, http://dx.doi.org/10.1016/j.commatsci.2021.110493.

[42] V. Ryzhii, M. Ryzhii, T. Otsuji, V. Mitin, M.S. Shur, Heat capacity of nonequilibrium electron-hole plasma in graphene layers and graphene bilayers, Phys. Rev. B 103 (24) (2021) 245414, http://dx.doi.org/10.1103/physrevb.103.245414.

[43] S. Lei, N. Su, M. Li, Thermal-resistance effect of graphene at high temperatures in nanoelectromechanical temperature sensors, Micromachines 13 (12) (2022) 2078, http://dx.doi.org/10.3390/mi13122078.

[44] S.M. Sze, K.K. Ng, Physics of Semiconductor Devices, third ed., John Wiley and Sons, Hoboken, NJ, 2006.

[45] C. Hu, Modern Semiconductor Devices for Integrated Circuits, first ed., Prentice Hall, Upper Saddle River, NJ, 2010.

[46] S. Tongay, M. Lemaitre, X. Miao, B. Gila, B.R. Appleton, A.F. Hebard, Rectification at graphene-semiconductor interfaces: Zero-gap semiconductor-based diodes, Phys. Rev. X 2 (1) (2012) 2160–3308, http://dx.doi.org/10.1103/PhysRevX.2.011002.

[47] SYNOPSYS, Sentaurus Device User Guide, version T-2022.03, 2022.

[48] Y.W. Sun, D. Holec, D. Gehringer, L. Li, O. Fenwick, D.J. Dunstan, C.J. Humphreys, Graphene on silicon: Effects of the silicon surface orientation on the work function and carrier density of graphene, Phys. Rev. B 105 (2022) 165416, http://dx.doi.org/10.1103/PhysRevB.105.165416.

[49] I.N. Yakovkin, Dirac cones in graphene, interlayer interaction in layered materials, and the band gap in MoS2, Crystals 6 (11) (2016) http://dx.doi.org/10.3390/cryst6110143.

[50] A.Y. Galashev, A.S. Vorob'ev, An ab initio study of the interaction of graphene and silicene with one-, two-, and three-layer planar silicon carbide, Phys. E: Low-Dimens. Syst. Nanostructures 138 (2022) 115120, http://dx.doi.org/10.1016/j.physe.2021.115120.

[51] C. Klein, D. Cohen-Elias, G. Sarusi, Controlling graphene work function by doping in a MOCVD reactor, Heliyon 4 (12) (2018) http://dx.doi.org/10.1016/j.heliyon.2018.e01030.

[52] A. Matković, M. Kratzer, B. Kaufmann, S.M. Sze, S.K. Nayak, A. Teichert, M. Gmitra, J. Fabian, U. Höfer, T. Valla, C. Teichert, Probing charge transfer between molecular semiconductors and graphene, Sci. Rep. 7 (2017) 9544, http://dx.doi.org/10.1038/s41598-017-09419-3.

[53] I. Shtepliuk, T. Iakimov, V. Khranovskyy, J. Eriksson, F. Giannazzo, R. Yakimova, Role of the potential barrier in the electrical performance of the graphene/SiC interface, Crystals 7 (6) (2017) 162, http://dx.doi.org/10.3390/cryst7060162.

[54] N.F. Mott, The theory of crystal rectifiers, Proc. R. Soc. Lond. Ser. A. Math. Phys. Sci. 171 (944) (1939) 27–38, http://dx.doi.org/10.1098/rspa.1939.0051.

[55] Y. Vaknin, R. Dagan, Y. Rosenwaks, Schottky barrier height and image force lowering in monolayer MoS2 field effect transistors, Nanomaterials 10 (12) (2020) 2346, http://dx.doi.org/10.3390/nano10122346.

[56] A. Alnuaimi, I. Almansouri, I. Saadat, A. Nayfeh, Interface engineering of graphene–silicon Schottky junction solar cells with an Al2O3 interfacial layer grown by atomic layer deposition, RSC Adv. 8 (19) (2018) 10593–10597, http://dx.doi.org/10.1039/c7ra13443f.

[57] J.K. Nangoi, C.J. Palmstrøm, C.G. Van De Walle, First-principles studies of Schottky barriers and tunneling properties at Al(111)/Si(111) and CoSi2(111)/Si(111) interfaces, Phys. Rev. B 110 (3) (2024) 035302, http://dx.doi.org/10.1103/physrevb.110.035302.